Contents lists available at ScienceDirect

Magnetic Resonance Imaging

Original contribution

7T GRE-MRI signal compartments are sensitive to dysplastic tissue in focal epilepsy

Kiran Thapaliya, Javier Urriola, Markus Barth, David C. Reutens, Steffen Bollmann, Viktor Vegh*

Centre for Advanced Imaging, University of Queensland, Queensland, Australia

A B S T R A C T

Ultra-high field magnetic resonance imaging data obtained using a multi-echo gradient echo sequence has been shown to contain information on tissue microstructure. Quantitative assessment of water fraction, relaxation time and frequency shift using multi-compartment signal modelling may help improve our understanding of diseases and disorders affecting the human brain. In this study, we explored tissue microstructure information by analysing voxel compartment water fraction and frequency shifts derived from 7 T multi-echo gradient recalled echo MRI data. We aimed to test whether the parameters of a three compartment model could distinguish the normal cortex from the cortex affected by focal cortical dysplasia. We compartmentalised normal and dysplastic cortical regions in patients diagnosed with focal cortical dysplasia. We found the frequency shift parameter of the shortest T_2^* signal compartment to be sensitive to regions of dysplastic tissue. We conclude that mathematical modelling of echo time dependent gradient recalled echo MRI signals in patients with focal cortical dysplasia can potentially delineate cortical areas that have undergone microstructural changes in comparison to normal tissue.

1. Introduction

Various types of focal cortical dysplasia (FCD) are developmental malformations of the cerebral cortex [1]. They are characterised by abnormal cortical architecture, with disruption of the normal organisation of the cortex into well-defined layers and potential blurring of the boundary between the cortex and the underlying white matter. White matter abnormalities are common in FCD and include reduced myelination or intrusion of neuronal cell bodies [2]. FCDs are often highly epileptogenic with approximately 75% of patients with FCD developing epilepsy [3], and 25–40% of all childhood-onset drug resistant epilepsies are caused by FCD [3–6]. Moreover, in 20–30% of patients with FCD, standard clinical MRI sequences do not reveal an identifiable lesion [7]. FCD has been classified into three types and multiple sub-types [1,8]. In FCD Type I, cortical lamination and/or columnar arrangement in grey matter are disrupted. Additionally, Type II FCD contains dysmorphic neurons or balloon cells. In FCD Type III, a second pathology such as hippocampal sclerosis, a tumour, a vascular malformation or another lesion acquired during early life is present.

Changes in cortical architecture have been detected using different non-invasive imaging technologies with the aim of localising epileptogenic tissue. The most sensitive non-invasive in vivo imaging technology for detecting FCD is MRI. Traditional clinical scans (< 7 T)

typically involve the collection of T_1- and T_2-weighted, and T_2 fluid-attenuated inversion recovery (FLAIR) MRI data [9–18]. T_1-weighted, T_2-weighted and FLAIR images have been used to estimate the volume, thickness and shape of features in the brain, based on having defined FCD lesion anatomical boundaries via changes in image intensity and contrast [13–15]. Voxel based methods have been used to measure the grey and white matter density [14,18], whilst surface or morphology based methods measure cortical thickness, sulcus depth, curvature, local gyrification index and MRI signal intensity variations [16,19]. However, existing MRI-based measures of changes in anatomy and morphology can be confounded by microstructural changes associated with FCD. These microstructural changes can effect both the grey and white matter MRI signal, making it difficult to quantify the effect due to FCD based on magnetic resonance images, which often are qualitative in nature [20,21]. Furthermore, FCDs can be difficult to distinguish from gliomas in T_2-weighted images [22]. Whilst gains in FCD detection rates can be made through the use of a multitude of MRI contrasts [23–25], a quantitative method that can potentially distinguish between dysplastic and normal tissue would help the current diagnostic procedure.

Gradient recalled echo (GRE)-MRI, a protocol sensitive to the magnetically inhomogeneous image voxel environment [26], can be used to generate quantitative information. In particular, multiple echo

time GRE-MRI data is routinely used to generate characteristic T_2^* relaxation times of tissue based on the temporal evolution of the GRE-MRI signal magnitude and, single echo time GRE-MRI signal phase images are the basis of quantitative magnetic susceptibility maps [27–29]. With the increased availability of 7 T MRI scanners, studies have focused on investigating the GRE-MRI signal phase and its relevance to mapping variations in tissue microstructure. Primary sources of changes in signal phase include tissue structure and composition, and content of iron, myelin, demyelination, ectopic neurons, glial proliferation and proteins [30–33]. It has been shown as well that tissue density, uniformity and orientation of axons affect the GRE-MRI signal phase in non-characteristic ways [27–29]. Whilst single echo time phase images are highly sensitive to the voxel tissue microenvironment, recent studies have demonstrated the potential of using multiple echo time phase images in conjunction with signal compartment modelling for the purpose of characterising the image voxel based on biological influences [34–40]. Building on existing findings, we used multi-echo GRE-MRI data and signal compartment modelling to test which compartment model parameters are sensitive to changes caused by FCD, and how well they differentiate between normal and FCD tissue.

2. Materials and methods

Ethics approval was granted by the Royal Brisbane and Women's Hospital and the University of Queensland, Brisbane, Australia, and written informed consent was obtained from 13 patients with clinically diagnosed FCD. Out of 13 patients, three patients showed clear FCD regions in FLAIR and MP2RAGE data acquired at 3 Tesla (3 T) and 7 T and one patient had suspected regions of FCD in fluid attenuated inversion recovery (FLAIR) and T1-weighted (MP2RAGE) data acquired at 7 T. Hence, four patient datasets were analysed (aged 42, 54, 32 and 33). Clinical data and patient characteristics for the four patients are summarised in Table 1. We also collected four healthy participant data (aged 34, 35, 25 and 35).

2.1. Data acquisition

MRI was performed on a 7 T whole body MRI research scanner (Siemens Healthcare, Erlangen, Germany) with a 32 channel head coil (Nova Medical Wilmington, USA). We acquired data using Magnetisation prepared 2 rapid acquisition gradient echoes (MP2RAGE), Fluid-attenuated inversion-recovery (FLAIR) and multi-echo gradient echo (GRE-MRI). MP2RAGE data were acquired using the following parameters: repetition time (TR) = 4300 ms, echo time (TE) = 3.44 ms, first inversion time (TI1) = 840 ms, TI2 = 2370 ms, first flip angle (FA1) = 5°, FA2 = 6° and resolution = 0.75 mm³ with matrix size = 300 × 320 × 256. FLAIR data were acquired using a turbo spins echo sequence with TR = 9000 ms, TE = 467 ms, TI = 2400 ms and resolution = 0.9 × 0.9 × 1 mm³ with matrix size = 284 × 256 × 192. Data were also acquired using a 3D GRE-MRI sequence using the following parameters: TEs from 5 ms to 30 ms with 3.13 ms echo spacing (9 echoes in total), TR = 48 ms and flip angle (FA) = 15°, voxel size was set to 0.75 mm³ with matrix size = 320 × 300 × 256. Two separate acquisitions were performed at 7 Tesla with and without the magnetisation transfer RF pulse. The first echo time data were used to compute magnetisation transfer ratio (MTR) images, provided as Supplementary material.

2.2. Data pre-processing

Our experience with multiple echo time data has been that both signal magnitude and phase evolve smoothly with echo time [40]. Hence, we reduced the number of echo times acquired and interpolated points between adjacent echo times. We created 17 echo point data using the standard function (interp) in MATLAB 2017b® by interpolating along the time dimension in every voxel. Phase unwrapping

Table 1
Clinical information and patient characteristic with FCD-like lesion on MRI scans for the four patients.

#	Age (years)	Sex (M/F)	Seizures over the last 6 months	Age (in years) of first epileptic symptoms	FCD region	MRI	EEG	PET
1	42	F	daily	4	Left central sulcus	Transmantle region underlying an area of FCD in the left frontal region	–	N/A
2	54	M	4 per week	4 or 6	Left parietal	Left parietal dysplasia	Left parietal seizure onset, Left parietal and central IEDs	N/A
3	32	M	3–4 every 6 months	1	Left parietal lobe epilepsy	Left parietal lobe dysplasia	–	N/A
4	33	F	5 per week	4.5	Left frontal	MRI negative 3 T / MRI positive 7 T?	Left anterior temporal and frontal IEDs	L Parietal hypometabolism

and background field removal was performed using iHARPERELLA (http://people.duke.edu/~cl160, STI Suite) [41]. We used the default parameters (iterations = 100; padsize = [100100100]) and a mask created from the first echo's magnitude image with the iHARPERELLA method to remove the background field. Signal magnitude and phase images generated for each echo time were used to form voxel-wise complex signals using our in-house MATLAB® scripts. Voxel signals were smoothed to 4D (3D space and 1D time) using the method of robust smoothing and by setting the smoothing kernel equal to 2 prior to voxel-wise analysis [42].

2.3. Three compartment model

We used an established three compartment model to parameterise the echo time dependent GRE-MRI signal evolution [37]:

$$S(t) = \left[S_1 e^{-\left(\frac{1}{T_{2,1}^*} + i2\pi\Delta f_1 \right)t} + S_2 e^{-\left(\frac{1}{T_{2,2}^*} + i2\pi\Delta f_2 \right)t} + S_3 e^{-\left(\frac{1}{T_{2,3}^*} + i2\pi\Delta f_3 \right)t} \right] e^{-i2\pi\Delta f_{bg}t},$$

(1)

where S_1, S_2 and S_3 represent signal amplitudes for the three signal compartments (first compartment - *C1*, second compartment - *C2* and third compartment - *C3*), and $T_{2,1}^*$, $T_{2,2}^*$ and $T_{2,3}^*$ and Δf_1, Δf_2 and Δf_3 are the corresponding signal compartment relaxation times and frequency shifts. Signal compartments were arranged by T_2^* values, from smallest to largest (i.e. smallest T_2^* value is C1). The exponential term at the end was used to model residual background effects not removed through the STI suite pipeline. The first compartment water fraction (*WF*) was computed using $WF_1 = \frac{S_1}{S_1 + S_2 + S_3}$. Water fractions for the second and third signal compartments were calculated in a similar manner. We fitted the signal model using the non-linear least squares fitting function (lsqnonlin) available in MATLAB, 2017b ®. Fitting bounds and initial values are provided in Table 2.

2.4. Region-of-interest analysis

Normal and FCD affected regions were manually segmented with the aid of MIPAV (https://mipav.cit.nih.gov) [43] by registering the MP2RAGE data onto the GRE-MRI magnitude data using FSL Flirt [44] from individual participants. FCD regions were segmented from MP2RAGE images where FCD areas were clearly visible and normal regions were selected from a non-FCD affected cortical region in the contralateral hemisphere, as shown in Fig. 1. Cortical regions were also segmented from the healthy participants and a region based analysis was performed. The complex signal was created by averaging pooled voxel signal from all ROIs (patient 1 FCD region, no. of voxel = 445, normal region = 121; patient 2, FCD region, no. of voxel = 1044, normal region = 206; patient 3, FCD region = 5478, normal region 734; patient 4, FCD region = 479, normal region = 362) and fitted using the model in [1] to obtain water fractions, relaxation times and frequency shifts from individual datasets. The data processing and analysis pipeline is shown in Fig. 2. The 95% confidence interval was created using region based values from healthy participants.

2.5. Voxel-wise maps of model parameters

A whole brain bask was created using the BET tool available in FSL [44]. At each echo time GRE-MRI magnitude and phase data were masked. Voxel-wise parameterisation of the complex echo time-dependent signal was performed for each voxel in the masked brain. Parameter maps were created by assigning the relevant parameter estimate to each voxel. Voxel-wise maps were assesed visually for differences in areas close to the FCD region.

3. Results

3.1. Region- of-interest analysis

The different tissue parameters (i.e. water fraction, relaxation time, and frequency shift) were estimated from the three-compartment model using [1] and we investigated whether the estimated parameters distinguish between normal and FCD cortical regions. The 95% confidence interval was created using the region based values from healthy participants. We plotted mean estimated water fraction, relaxation time and frequency shifts values of each compartment (Figs. 3 and 4; solid lines) and the 95% confidence interval (Figs. 3 and 4; dashed lines) calculated from healthy participants. We observed that first compartment frequency shift values of FCD regions were outside the 95% confidence interval compared to the normal appearing region in three patients and lower in a one patient. We observed that the first compartment frequency shift estimated in FCD regions did not fall within the range of 95% confidence interval whereas second and third compartment frequency shift values were in the range of 95% confidence interval for FCD as well as for normal appearing region as shown in Fig. 3. We also plotted water fractions and relaxation time of each compartment against 95% confidence interval. We found that these tissue parameters were within the range of 95% confidence interval with higher between patient variability shown in Fig. 4. The water fraction and relaxation time tissue parameters were found to be undistinguishable between FCD and normal appearing cortical regions in all patients.

The first compartment frequency shifts were consistent across the normal cortical brain regions in all patients (ranging from 18 Hz to 22 Hz). The frequency shifts for the other two compartments (i.e. second and third) for all patients were similar (C2: 10 Hz to 12 Hz; C3: 19 to 21 Hz). The first compartment frequency shifts in FCD regions ranged from 36 Hz to 46.13 Hz in three patients and a lower frequency shift was observed for the fourth patient (11 Hz). The FCD region-specific frequency shifts for the second and third signal compartments for all patients were also similar (C2: 9 Hz to 10 Hz; C3: 18 Hz to 21 Hz). The frequency shift estimated for normal and FCD regions in all patients showed clear differences only in the first signal compartment, as shown in Table 3. The decay curves for fitting FCD and normal regions have been provided as Supplementary material.

The goodness-of-fit was measured by estimating the standard error rate in percentage, as shown in Table 3. The computed error rate for the FCD regions is slightly higher than normal regions. The

Table 2
Initial values and search ranges for model parameters. We state amplitudes for the three compartments as a percentage of the signal magnitude at the first echo time.

	S_1 (%)	S_2 (%)	S_3 (%)	$T_{2,1}^*$ (ms)	$T_{2,2}^*$ (ms)	$T_{2,3}^*$ (ms)	Δf_1 (Hz)	Δf_2 (Hz)	Δf_3 (Hz)	Δf_{bg} (Hz)
Initial value	50	50	50	7	50	30	25	10	25	−10
Lower bound	0	0	0	1	1	1	1	1	1	−40
Upper bound	100	100	100	15	200	200	∞	30	40	10

Table 3
The summary of the estimated frequency shift (Δf in Hz) for each compartment and the standard error (%) calculated for normal and FCD regions.

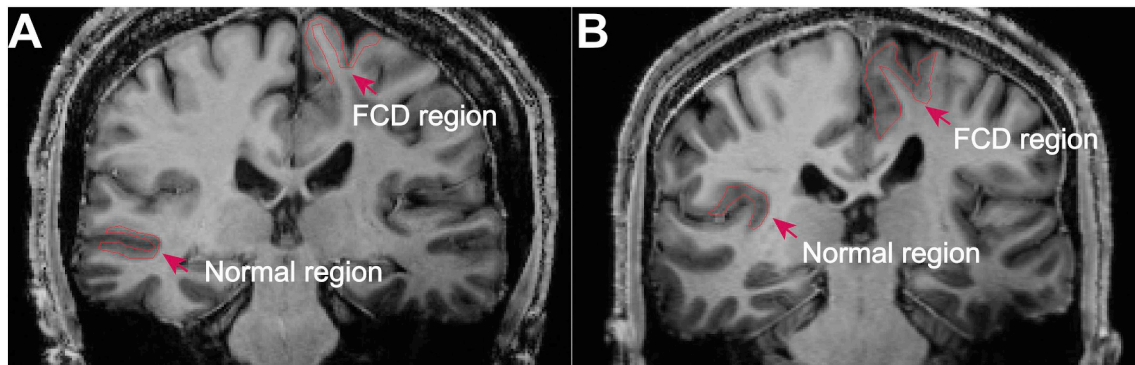| Patient	Normal region Frequency shift (Δf in Hz)			FCD region Frequency shift (Δf in Hz)			Standard error (%)	
	C1	C2	C3	C1	C2	C3	Normal region	FCD region
1	22	12	21	36	9	20	1	4
2	18	11	20	38	11	21	1	1
3	21	10	19	46	9	20	0.4	4
4	19	11	19	11	10	18	0.4	1

Fig. 1. Illustration of normal and FCD regions of two patients (A and B). Such ROIs across consecutive slices of the MP2RAGE data were used in the region-based analysis. Please note that here we are showing examples of segmentations, and the contralateral sides to the FCD regions were used as well where possible.

overall error rates for all patients are < 4% in the FCD regions and < 1% in normal regions.

3.2. Voxel-based analysis

Fig. 5 shows the voxel by voxel fit results for the first signal compartment frequency shift in four FCD patients. The voxel-by-voxel maps of frequency shift values show differences between the dysplastic and normal tissue in the first compartment (C1).

Interestingly for Patient 1, with a clearly presenting transmantle sign (Fig. 5, red arrow), the largest increase in frequency shift co-localises with the grey matter region of high cortical curvature. In addition, increases in frequency shift can also be observed around the transmantle sign, which may be suggestive of dysplastic tissue to a lower extent than at the transmantle region. In Patient 2 the region of elevated frequency shifts (red arrows) correspond with the region of apparent atrophy across both hemispheres in the parietal region of the brain. In Patient 3 the obvious parietal region atrophy on the right extends to the temporo-parietal junction on the left, with the highest frequency shift concentrated towards the top of the head. In Patient 4, suspected FCD regions were notable only in the 7 T scanner in both FLAIR and MP2RAGE images. The first compartment frequency shift in this region were smaller in comparison to the regions of the other three FCD patients. It was difficult to locate the FCD regions for patient 4 which has a similar first compartment frequency shift in comparison to the normal regions.

4. Discussion

In focal epilepsy brain regions affected by FCD have been shown to correspond with seizure onset. Whilst EEG can be used to monitor abnormal brain activity, it is not highly specific to brain regions and cannot be used to delineate regions affected by FCD. MRI methods play a key role in the delineation of FCD. In fact, MRI has revolutionised presurgical workup by enabling non-invasive visualisation of FCDs. Accurate pre-surgical delineation of FCD provides seizure freedom for 60–80% of patients after surgery versus 30–40% success rate for MRI-negative patients [45–47]. However, a major challenge remains, since visual analysis of conventional MRI scans (i.e. T1- and T2-weighted clinical scans) is normal in 20–40% of patients with some forms of FCD [6]. Technological gains, such as ultra-high field human imaging (i.e. ≥ 7 T MRI) and new imaging methods which derive novel image contrasts from tissue microstructure influences on the complex valued echo-time dependent GRE-MRI signal, offer new possibilities to improve the detection of FCD.

We used signal compartmentalisation of the GRE-MRI signal and assessed how model parameters change in normal and FCD regions of the brain. Using ROI-based analysis, water fraction and relaxation time did not show any changes in the FCD regions. We found the frequency shift

parameter of the first signal compartment (defined as the signal compartment with the smallest T_2^* value) to change due to FCD. Our region-based as well as voxel-wise results showed increased frequency shift in three confirmed FCD patients from MR and lower frequency shift in one suspected FCD patient. We attribute an increase in frequency shift of the confirmed FCD regions in the first compartment to the presence of dysplastic tissue, which may be more diffuse than observable on clinical scans. The parameterisation of multiple echo time GRE-MRI data may lead to improved assessment of regions affected by FCD.

4.1. Causes of increased frequency shifts

The underlying causes leading to a change in frequency shift between normal and FCD cortical regions are unknown. However, a higher frequency shift in the FCD region could be caused by tissue microstructure abnormalities [28], iron deposition and accumulation, fibre breakdown, and calcification [28,48–51]. Wiggermann et al. found higher frequency shifts in multiple sclerosis lesions compared to normal appearing white matter, which was attributed to demyelination, deposition of tissue debris, the presence of various cells, such as macrophages, reactive astrocytes, and non-macrophage inflammatory cells, and an expansion of the extracellular space [51]. Others have shown analytically that demyelination and remyelination processes in multiple sclerosis can lead to substantial increases in frequency shifts [28]. The increase in first compartment frequency shifts in three patients found using our analysis could therefore be due to the changes in tissue structure, increase in tissue debris and the presence of various cells, such as macrophages, reactive astrocytes, and non-macrophage inflammatory cells. An increase in frequency shift in the FCD regions could also be due to an expansion of the extracellular space and indistinctness of the grey and white matter junction [52]. The suspected region of FCD in patient 4 has lower frequency shift in comparison to other three patients which could be due to the different kinds of tissue microstructure present in different FCD types [53,54].

4.2. Inter-patient variability

Whilst the general trend of increased frequency shift in the first compartment was present in three patients, the amount of change varied across patients (see Fig. 3). This difference in the amount of change in frequency shift between normal and FCD regions in a single patient could be due to tissue microstructure differences for different FCD types [53–56]. In FCD Type II, for example, the formation of balloon cells is present. These cells are generally large (tens of μm to as large as 80 μm in size) in comparison to surroundings (on the μm scale). As such, balloon cells, the formation of differently shaped and sized dysmorphic neurons and expansion of the extracellular space could lead to differences in frequency shifts [8,52]. Any differences in frequency shifts for the normal brain regions could be explained by expected
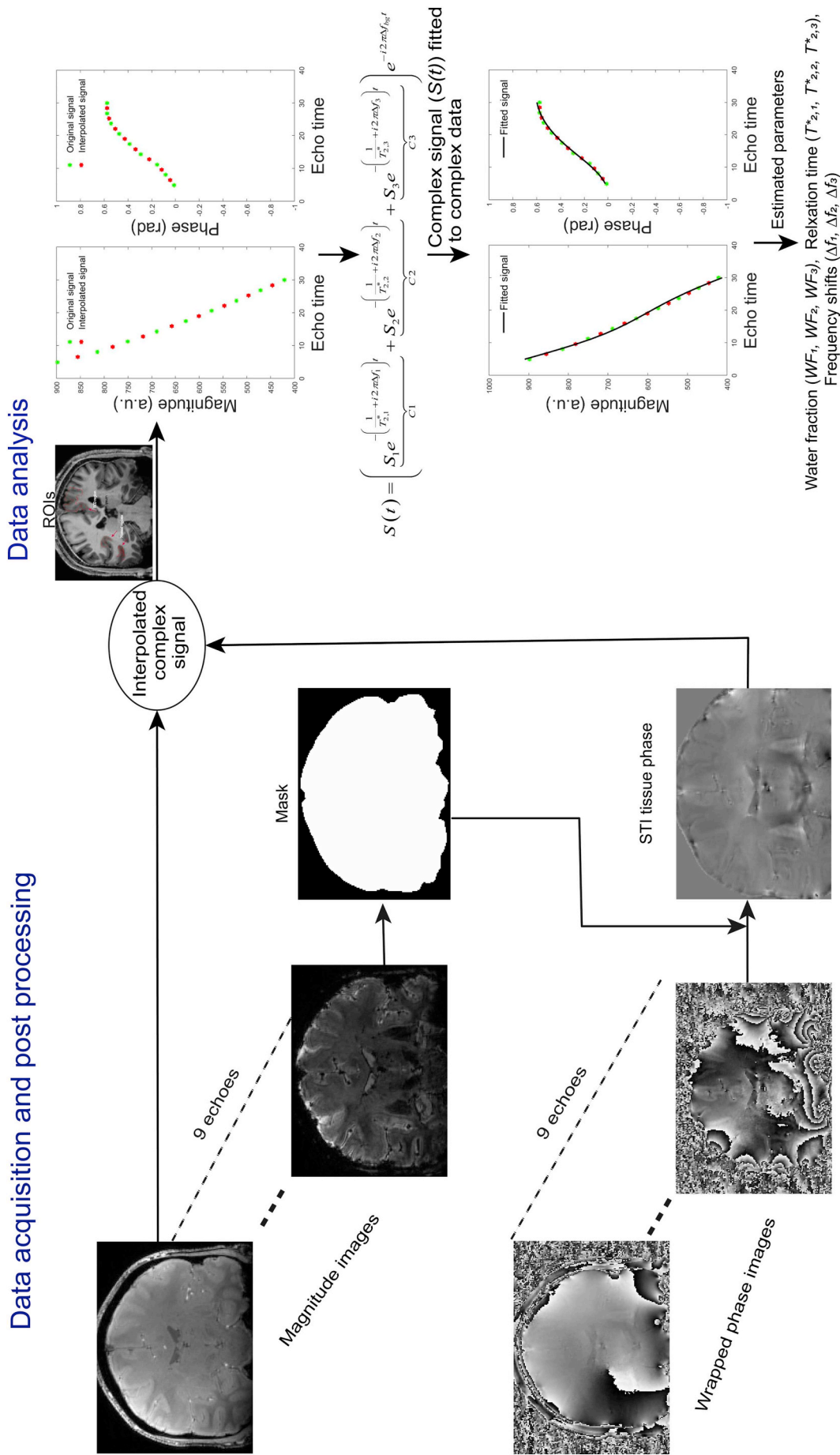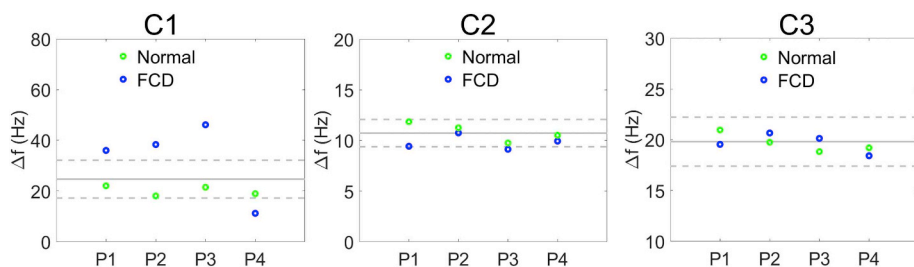
Fig. 2. Illustrated are the steps involved in computing the signal compartment model parameters. Data acquisition and post processing are shown on the left and data analysis steps on the right. The complex signal was generated from signal magnitude and tissue phase, before fitting the complex signal $S(t)$. The result of this process is the estimation of the various model parameters (i.e. water fraction- WF_1, WF_2 and WF_3, relaxation time- $T_{2,1}^*$, $T_{2,2}^*$ and $T_{2,3}^*$, frequency shift-Δf_1, Δf_2 and Δf_3).

Fig. 3. Illustration of frequency shift (C1-first compartment, C2-second compartment, and C3-third compartment) in the normal and FCD regions for the four patients computed via signal compartmentalisation. The x-axis identifies each participant (P1-P4) and the y-axis depicts the frequency shift (Δf in Hz). The solid line represents the healthy participant mean values, and the dotted lines the 95% confidence interval region. The confidence intervals were generated from anatomically similar cortical regions segmented from healthy participants. The blue circles represent the frequency shift estimated in FCD regions whereas green circles represent the frequency shift estimated in normal regions. (For interpretation of the references to colour in this figure legend, the reader is referred to the web version of this article.)
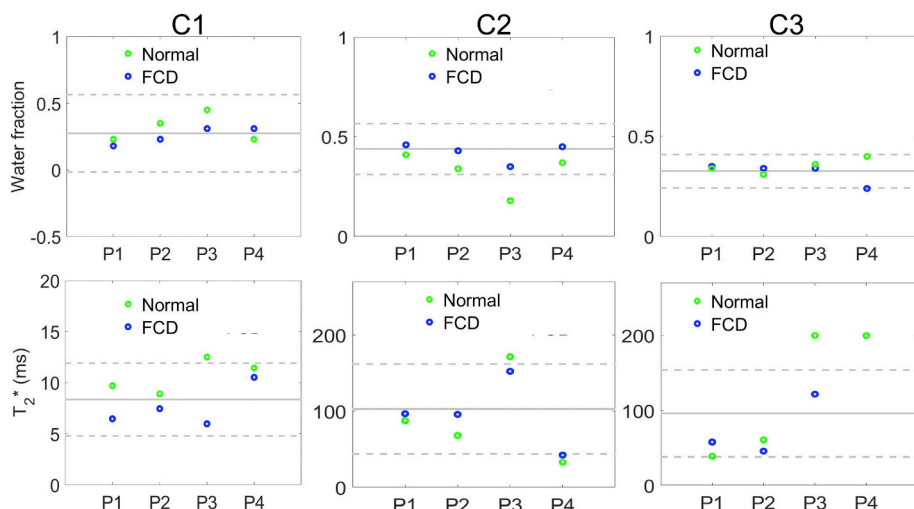
Fig. 4. Illustration of water fraction (top row) and relaxation time (bottom row) in the normal and FCD regions for the four patients computed via signal compartmentalisation. The x-axis identifies each participant (P1-P4), the y-axis depicts the water fraction (top row) and T_2^* relaxation time in milliseconds (bottom row). C1, C2 and C3 are the first, second and third compartment respectively. The solid line represents the healthy participant mean values, and the dotted lines highlight the 95% confidence interval region. The confidence intervals were generated from anatomically similar cortical regions segmented from healthy participants.
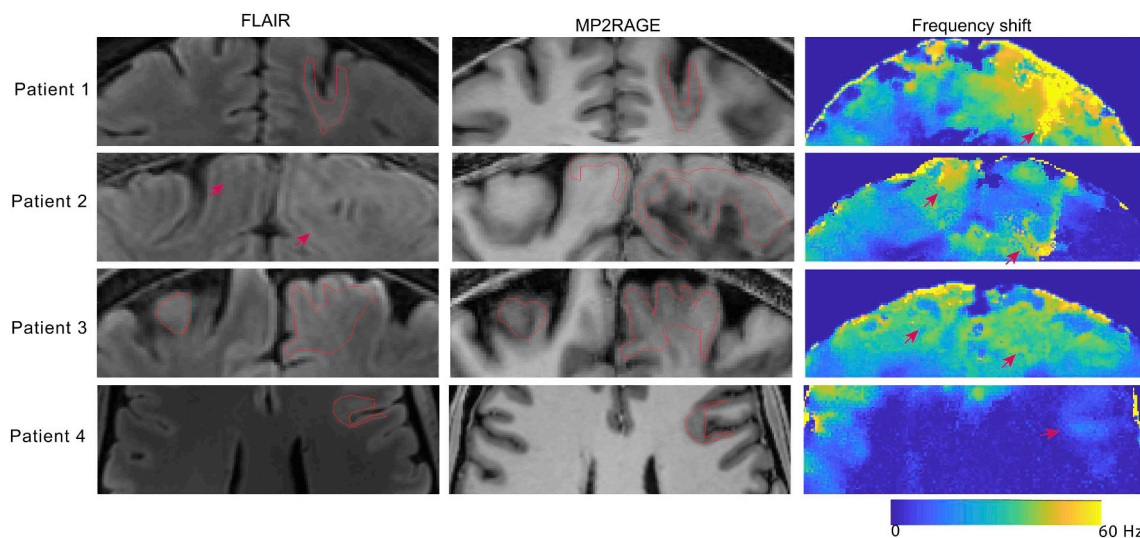
Fig. 5. The FLAIR, MP2RAGE and voxel-wise mapping of first compartment frequency shifts for four FCD patients. FCD regions were drawn in FLAIR and MP2RAGE where possible and shown by arrows, if FCD regions are not clearly distinguishable (Patient 2, FLAIR). Red arrows depict the first compartment frequency shift in the location of the FCD regions in Patient 1–4 corresponding to regions of brain atrophy shown in FLAIR and MP2RAGE. (For interpretation of the references to colour in this figure legend, the reader is referred to the web version of this article.)

variations in frequency shifts across participants, as established previously [39,40].

Three different types of FCD have been defined in the literature, with multiple sub-types [1]. Each type of FCD has different microstructural features, and in our study we did not have a diagnosis of FCD type. Therefore, we speculate that patient 4 has a different subtype of FCD and as such exhibits a different characteristic in terms of compartment model parameters (refer to Figs. 3–5).

4.3. Limitations of the study

The frequency shift in the tissue has been shown to be affected by fibre orientation [27,57], not accounted for by the model used in this research. The GRE-MRI signal phase has a considerably higher contrast-to-noise ratio at 7 T than the GRE-MRI signal magnitude [28]. However, raw phase images generated by the scanner require post processing which needs to be standardised and different processing techniques

may influence the estimated values [58]. Hence, different reconstruction pipelines could be investigated in the future to further improve the quality of results. One such possibility is the use of established quantitative susceptibility mapping pipelines, to be able to convert non-local tissue phase into local susceptibilities and then into local frequency shifts [39,40]. We report the frequency information for normal and FCD regions at a single imaging time point. Longitudinal studies may reveal how frequency shifts change over time and how different regions may evolve. Future longitudinal research on a larger cohort could show whether frequency shifts mapped using GRE-MRI signal compartment modelling can be used to detect global changes on the FCD affected cortex.

5. Conclusion

Based on the estimation of three compartment tissue parameters from multiple echo time gradient recalled echo MRI data, the frequency shift of the shortest T_2^* value signal compartment was found higher in three FCD patients and lower in a fourth patient. Other tissue parameters like water fraction and relaxation time did not show clear distinction between normal and FCD regions. A higher frequency shift in the FCD region appears to reflect a change in tissue microstructure, a previous effect established on the echo time dependent GRE-MRI signal. Overall, our findings suggest that frequency shift could be a sensitive tissue parameter in cortical malformations associated with FCD.

Acknowledgements

Appendix A. Supplementary data

Supplementary data to this article can be found online at https://doi.org/10.1016/j.mri.2019.05.011.

References

[1] Najm IM, Sarnat HB, Blümcke I. Review: the international consensus classification of focal cortical dysplasia – a critical update 2018. Neuropathol Appl Neurobiol 2018;44(1):18–31. (Feb 1).

[2] Besson P, Andermann F, Dubeau F, Bernasconi A. Small focal cortical dysplasia lesions are located at the bottom of a deep sulcus. Brain 2008;131(12):3246–55. Dec 1.

[3] Semah F, Picot MC, Adam C, Broglin D, Arzimanoglou A, Bazin B, et al. Is the underlying cause of epilepsy a major prognostic factor for recurrence? Neurology 1998;51(5):1256–62. Nov.

[4] Wyllie E, Comair YG, Kotagal P, Bulacio J, Bingaman W, Ruggieri P. Seizure outcome after epilepsy surgery in children and adolescents. Ann Neurol 1998;44(5):740–8. Nov 1.

[5] McGonigal A, Bartolomei F, Régis J, Guye M, Gavaret M, Fonseca AT-D, et al. Stereoelectroencephalography in presurgical assessment of MRI-negative epilepsy. Brain 2007;130(12):3169–83. Dec 1.

[6] Berg AT, Vickrey BG, Langfitt JT, Sperling MR, Walczak TS, Shinnar S, et al. The multicenter study of epilepsy surgery: recruitment and selection for surgery. Epilepsia 2003;44(11):1425–33. Nov 1.

[7] Duncan JS. Imaging in the surgical treatment of epilepsy. Nat Rev Neurol 2010;6(10):537–50. Oct.

[8] Blümcke I, Thom M, Aronica E, Armstrong DD, Vinters HV, Palmini A, et al. The clinicopathologic spectrum of focal cortical dysplasias: a consensus classification proposed by an ad hoc Task Force of the ILAE Diagnostic Methods Commission 1.

[9] Bernasconi A, Bernasconi N, Bernhardt BC, Schrader D. Advances in MRI for "cryptogenic" epilepsies. Nat Rev Neurol 2011;7(2):99. Feb.

[10] Leach JL, Greiner HM, Miles L, Mangano FT. Imaging spectrum of cortical dysplasia in children. Semin Roentgenol 2014;49(1):99–111. (Jan 1).

[11] Mellerio C, Labeyrie M-A, Chassoux F, Roca P, Alami O, Plat M, et al. 3T MRI improves the detection of transmantle sign in type 2 focal cortical dysplasia. Epilepsia 2014;55(1):117–22. (Jan 1).

[12] Mellerio C, Labeyrie M-A, Chassoux F, Daumas-Duport C, Landre E, Turak B, et al. Optimizing MR imaging detection of type 2 focal cortical dysplasia: best criteria for clinical practice. Am J Neuroradiol 2012;33(10):1932–8. Nov 1.

[13] Guerrini R, Duchowny M, Jayakar P, Krsek P, Kahane P, Tassi L, et al. Diagnostic methods and treatment options for focal cortical dysplasia. Epilepsia 2015;56(11):1669–86. Nov 1.

[14] House PM, Lanz M, Holst B, Martens T, Stodieck S, Huppertz H-J. Comparison of morphometric analysis based on T1- and T2-weighted MRI data for visualization of focal cortical dysplasia. Epilepsy Res 2013;106(3):403–9. Oct 1.

[15] Adler S, Lorio S, Jacques TS, Benova B, Gunny R, Cross JH, et al. Towards in vivo focal cortical dysplasia phenotyping using quantitative MRI. NeuroImage Clin 2017;15:95–105.

[16] Ahmed B, Brodley CE, Blackmon KE, Kuzniecky R, Barash G, Carlson C, et al. Cortical feature analysis and machine learning improves detection of "MRI-negative" focal cortical dysplasia. Epilepsy Behav 2015;48(Supplement C):21–8. Jul 1.

[17] Hong S-J, Bernhardt BC, Schrader DS, Bernasconi N, Bernasconi A. Whole-brain MRI phenotyping in dysplasia-related frontal lobe epilepsy. Neurology 2016;86(7):643. Feb 16.

[18] Huppertz H-J, Grimm C, Fauser S, Kassubek J, Mader I, Hochmuth A, et al. Enhanced visualization of blurred gray–white matter junctions in focal cortical dysplasia by voxel-based 3D MRI analysis. Epilepsy Res 2005;67(1):35–50. Oct 1.

[19] Adler S, Wagstyl K, Gunny R, Ronan L, Carmichael D, Cross JH, et al. Novel surface features for automated detection of focal cortical dysplasias in paediatric epilepsy. NeuroImage Clin 2017;14(Supplement C):18–27. Jan 1.

[20] Glasser MF, Essen DCV. Mapping human cortical areas in vivo based on myelin content as revealed by T1- and T2-weighted MRI. J Neurosci 2011;31(32):11597–616. Aug 10.

[21] Scholtens LH, de Reus MA, van den Heuvel MP. Linking contemporary high resolution magnetic resonance imaging to the von economo legacy: a study on the comparison of MRI cortical thickness and histological measurements of cortical structure. Hum Brain Mapp 2015;36(8):3038–46. Aug 1.

[22] Razek AAKA, Kandell AY, Elsorogy LG, Elmongy A, Basett AA. Disorders of cortical formation: MR imaging features. Am J Neuroradiol 2009;30(1):4–11. Jan 1.

[23] Rugg-Gunn FJ, Eriksson SH, Boulby PA, Symms MR, Barker GJ, Duncan JS. Magnetization transfer imaging in focal epilepsy. Neurology 2003;60(10):1638–45. May 27.

[24] Rugg-Gunn FJ, Boulby PA, Symms MR, Barker GJ, Duncan JS. Imaging the neocortex in epilepsy with double inversion recovery imaging. NeuroImage 2006;31(1):39–50. May 15.

[25] Saini J, Singh A, Kesavadas C, Thomas B, Rathore C, Bahuleyan B, et al. Role of three-dimensional fluid-attenuated inversion recovery (3D FLAIR) and proton density magnetic resonance imaging for the detection and evaluation of lesion extent of focal cortical dysplasia in patients with refractory epilepsy. Acta Radiol Stockh Swed 1987 2010;51(2):218–25. Mar.

[26] Yablonskiy DA, Haacke EM. Theory of NMR signal behavior in magnetically inhomogeneous tissues: the static dephasing regime. Magn Reson Med 1994;32(6):749–63. (Dec 1).

[27] Wharton S, Bowtell R. Gradient echo based fiber orientation mapping using R2* and frequency difference measurements. NeuroImage 2013;83:1011–23. Dec.

[28] He X, Yablonskiy DA. Biophysical mechanisms of phase contrast in gradient echo MRI. Proc Natl Acad Sci 2009;106(32):13558–63. Aug 11.

[29] Duyn JH, van Gelderen P, Li T-Q, de Zwart JA, Koretsky AP, Fukunaga M. High-field MRI of brain cortical substructure based on signal phase. Proc Natl Acad Sci 2007;104(28):11796–801. Jul 10.

[30] Luo J, Jagadeesan BD, Cross AH, Yablonskiy DA. Gradient echo plural contrast imaging – signal model and derived contrasts: T2*, T1, phase, SWI, T1f, FST2*and T2*-SWI. Neuroimage 2012;60(2):1073–82. (Apr 2).

[31] Lee J, Shmueli K, Kang B-T, Yao B, Fukunaga M, van Gelderen P, et al. The contribution of myelin to magnetic susceptibility-weighted contrasts in high-field MRI of the brain. NeuroImage 2012;59(4):3967–75. Feb 15.

[32] Lodygensky GA, Marques JP, Maddage R, Perroud E, Sizonenko SV, Hüppi PS, et al. In vivo assessment of myelination by phase imaging at high magnetic field. NeuroImage 2012;59(3):1979–87. Feb 1.

[33] Liu C, Li W, Johnson GA, Wu B. High-field (9.4 T) MRI of brain dysmyelination by quantitative mapping of magnetic susceptibility. NeuroImage 2011;56(3):930–8. Jun 1.

[34] Hwang D, Kim D-H, Du YP. In vivo multi-slice mapping of myelin water content using T2* decay. NeuroImage 2010;52(1):198–204. (Aug 1).

[35] van Gelderen P, de Zwart JA, Lee J, Sati P, Reich DS, Duyn JH. Nonexponential T2* decay in white matter. Magn Reson Med 2012;67(1):110–7. (Jan 1).

[36] Sati P, van Gelderen P, Silva AC, Reich DS, Merkle H, de Zwart JA, et al. Microcompartment specific T2∗ relaxation in the brain. NeuroImage 2013;77:268–78. Aug 15.

[37] Nam Y, Lee J, Hwang D, Kim D-H. Improved estimation of myelin water fraction using complex model fitting. NeuroImage 2015;116:214–21. Aug 1.

[38] Thapaliya K, Vegh V, Bollmann S, Barth M. Assessment of microstructural signal compartments across the corpus callosum using multi-echo gradient recalled echo at 7 T. NeuroImage 2018;182:407–16.

[39] Sood S, Urriola J, Reutens D, O'Brien K, Bollmann S, Barth M, et al. Echo time-dependent quantitative susceptibility mapping contains information on tissue properties. Magn Reson Med 2016 May 1;77:1946–58.

[40] Kadamangudi S, Reutens D, Sood S, Vegh V. Signal compartments in ultra-high field multi-echo gradient echo MRI reflect underlying tissue microstructure in the brain. NeuroImage 2018;178:403–13. Sep 1.

[41] Li W, Avram AV, Wu B, Xiao X, Liu C. Integrated Laplacian-based phase unwrapping and background phase removal for quantitative susceptibility mapping. NMR Biomed 2014;27(2):219–27. Feb 1.

[42] Garcia D. Robust smoothing of gridded data in one and higher dimensions with missing values. Comput Stat Data Anal 2010;54(4):1167–78. Apr 1.

[43] McAuliffe MJ, Lalonde FM, McGarry D, Gandler W, Csaky K, Trus BL. Medical image processing, analysis and visualization in clinical research. 14th IEEE symposium on computer-based medical systems, 2001 CBMS 2001 proceedings. 2001. p. 381–6.

[44] Smith SM, Jenkinson M, Woolrich MW, Beckmann CF, Behrens TEJ, Johansen-Berg H, et al. Advances in functional and structural MR image analysis and implementation as FSL. NeuroImage 2004;23:S208–19. Jan 1.

[45] Téllez-Zenteno JF, Hernández-Ronquillo L. A review of the epidemiology of temporal lobe epilepsy [internet]. Epilepsy research and treatment. 2012 [cited 2018 Aug 29. Available from: https://www.hindawi.com/journals/ert/2012/630853/].

[46] Wieshmann UC, Larkin D, Varma T, Eldridge P. Predictors of outcome after temporal lobectomy for refractory temporal lobe epilepsy. Acta Neurol Scand 2008;118(5):306–12. Nov 1.

[47] Stavem K, Bjørnæs H, Langmoen IA. Predictors of seizure outcome after temporal lobectomy for intractable epilepsy. Acta Neurol Scand 2004;109(4):244–9. Apr 1.

[48] Haacke EM, Makki M, Ge Y, Maheshwari M, Sehgal V, Hu J, et al. Characterizing iron deposition in multiple sclerosis lesions using susceptibility weighted imaging. J Magn Reson Imaging 2009;29(3):537–44. Mar 1.

[49] Hammond KE, Metcalf M, Carvajal L, Okuda DT, Srinivasan R, Vigneron D, et al. Quantitative in vivo magnetic resonance imaging of multiple sclerosis at 7 Tesla with sensitivity to iron. Ann Neurol 2008;64(6):707–13. Dec 1.

[50] Khalil M, Enzinger C, Langkammer C, Tscherner M, Wallner-Blazek M, Jehna M, et al. Quantitative assessment of brain iron by R2* relaxometry in patients with clinically isolated syndrome and relapsing–remitting multiple sclerosis. Mult Scler J 2009 Sep 1;15(9):1048–54.

[51] Wiggermann V, Hernández Torres E, Vavasour IM, Moore GRW, Laule C, MacKay AL, et al. Magnetic resonance frequency shifts during acute MS lesion formation. Neurology 2013;81(3):211–8. Jul 16.

[52] Bronen RA, Vives KP, Kim JH, Fulbright RK, Spencer SS, Spencer DD. Focal cortical dysplasia of Taylor, balloon cell subtype: MR differentiation from low-grade tumors. AJNR Am J Neuroradiol 1997;18(6):1141–51. Jul.

[53] Callaghan MF, Freund P, Draganski B, Anderson E, Cappelletti M, Chowdhury R, et al. Widespread age-related differences in the human brain microstructure revealed by quantitative magnetic resonance imaging. Neurobiol Aging 2014;35(8):1862–72. Aug.

[54] Carey D, Caprini F, Allen M, Lutti A, Weiskopf N, Rees G, et al. Quantitative MRI provides markers of intra-, inter-regional, and age-related differences in young adult cortical microstructure. NeuroImage [Internet]. [cited 2017 Dec 6]; Available from: https://www.sciencedirect.com/science/article/pii/S1053811917310121

[55] Yeatman JD, Wandell BA, Mezer AA. Lifespan maturation and degeneration of human brain white matter. Nat Commun 2014 Sep 17;5:4932.

[56] Whitaker KJ, Vértes PE, Romero-Garcia R, Váša F, Moutoussis M, Prabhu G, et al. Adolescence is associated with genomically patterned consolidation of the hubs of the human brain connectome. Proc Natl Acad Sci 2016;113(32):9105–10. Aug 9.

[57] Wharton S, Bowtell R. Fiber orientation-dependent white matter contrast in gradient echo MRI. Proc Natl Acad Sci U S A 2012;109(45):18559–64. Nov 6.

[58] Cronin MJ, Wang N, Decker KS, Wei H, Zhu W-Z, Liu C. Exploring the origins of echo-time-dependent quantitative susceptibility mapping (QSM) measurements in healthy tissue and cerebral microbleeds. NeuroImage 2017;149:98–113. Apr 1.